

## Article

# Study on Vibration and Noise of Railway Steel–Concrete Composite Box Girder Bridge Considering Vehicle–Bridge Coupling Effect

Jinyan Si <sup>1</sup>, Li Zhu <sup>2,\*</sup> , Weitao Ma <sup>2</sup>, Bowen Meng <sup>2</sup>, Huifeng Dong <sup>2</sup>, Hongyang Ning <sup>2</sup> and Guanyuan Zhao <sup>2</sup><sup>1</sup> Beijing Municipal Engineering Institute, Beijing 100037, China<sup>2</sup> School of Civil Engineering, Beijing Jiaotong University, Beijing 100044, China

\* Correspondence: zhuli@bjtu.edu.cn

**Abstract:** A steel–concrete composite beam bridge fully exploits the mechanical advantages of the concrete structure and steel structure, and has the advantages of a fast construction speed and large stiffness. It is of certain research value to explore the application of this bridge type in the field of railway bridges. However, with the rapid development of domestic high-speed railway construction, the problem of vibration and noise radiation of high-speed railway bridges caused by train loads is becoming more and more serious. A steel–concrete composite beam bridge combines the tensile characteristics of steel and the compressive characteristics of concrete perfectly. At the same time, it also has the characteristics of a steel bridge and concrete bridge in terms of vibration and noise radiation. This feature makes the study of the vibration and noise of the bridge type more complicated. Therefore, in this paper, the characteristics of vibration and noise radiation of a high-speed railway steel–concrete composite box girder bridge are studied in detail from two aspects: the theoretical basis and a numerical simulation. The main results obtained are as follows: Relying on the idea of vehicle–rail–bridge coupling dynamics, a structural dynamics analysis model of a steel–concrete combined girder bridge for a high-speed railroad was established, and numerical program simulation of the vibration of the vehicle–rail–bridge coupling system was carried out based on the parametric design language of ANSYS 18.0 and the language of MATLAB R2021a, and the structural vibration results were analyzed in both the time domain and frequency domain. By using different time-step loading for the vehicle–rail–bridge coupling vibration analysis, the computational efficiency can be effectively improved under the condition of guaranteeing the accuracy of the result analysis within 100 Hz. Based on the power flow equilibrium equation, a statistical energy method of calculating the high-frequency noise radiation is theoretically derived. Based on the theoretical basis of the statistical energy method, the high-frequency noise in the structure is numerically simulated in the VAONE 2021 software, and the average contribution of the concrete roof plate to the three acoustic field points constructed in this paper is as high as 50%, which is of great significance in the study of noise reduction in steel–concrete composite girders.

**Keywords:** vehicle–track–bridge coupling dynamics; steel–concrete composite beam; statistical energy method



**Citation:** Si, J.; Zhu, L.; Ma, W.; Meng, B.; Dong, H.; Ning, H.; Zhao, G. Study on Vibration and Noise of Railway Steel–Concrete Composite Box Girder Bridge Considering Vehicle–Bridge Coupling Effect. *Buildings* **2024**, *14*, 2509. <https://doi.org/10.3390/buildings14082509>

Academic Editor: Fabrizio Gara

Received: 24 July 2024

Revised: 8 August 2024

Accepted: 10 August 2024

Published: 14 August 2024



**Copyright:** © 2024 by the authors. Licensee MDPI, Basel, Switzerland. This article is an open access article distributed under the terms and conditions of the Creative Commons Attribution (CC BY) license (<https://creativecommons.org/licenses/by/4.0/>).

## 1. Introduction

Since the 1990s, there has been significant progress in both the practical application and theoretical understanding of composite beams [1]. Composite beams have been extensively utilized in foreign railway bridge construction during this period [2–6]. Since the year 2000, there has been significant progress in the construction of domestic railway systems, leading to the use of steel–concrete composite beams in numerous railway bridges inside the country [7–9]. Railway bridges experience a greater magnitude and more frequent external load compared to highway bridges. The issue of vibration and noise emission from bridges under these loads holds significant research importance.

Trains operating at high velocities on bridges can induce bridge vibration, and the potent dynamic impacts can readily result in structural harm or even bridge collapse. In 1849, Willis [10] and Stokes [11] derived an approximate and analytical solution to the equations governing bridge vibrations. They achieved this by disregarding the mass of the bridge and simplifying the locomotive as a moving load. Krylov [12] and Timoshenko [13,14] conducted analytical studies on the vibration issue of bridges. They took into account the bridge bulk and simplified the train loads as either moving concentrated forces or simple harmonic forces, respectively. Inglis [15] formulated differential equations that describe the vertical vibration of a vehicular bridge system and derived an approximate solution. In his analysis, he took into account the masses of both the bridge and the vehicle, and also considered the vehicle load as a periodic inertia force that moves. Owing to the constraints of computing technology, numerous simplifications of the theoretical parts of the model resulted in a substantial discrepancy between the analytical findings and practical outcomes.

In the 1960s, computer technology developed rapidly. Matsuura [16] considered the secondary spring suspension of locomotives and established a more refined locomotive model. For a total of ten degrees of freedom, this model took into account the heaving vibrations of the four wheel pairs as well as the nodding and heaving vibrations of the car body and bogie. Chu et al. [17,18] expanded the problem to three dimensions and developed a vehicle model with 11 degrees of freedom. A spatial motion model of the vehicle–bridge system was built using this specific vehicle model. Bhatti [19] introduced a vehicle model that covers 21 degrees of freedom, where track irregularity serves as the source of excitation. Wang [20] enhanced the previous concept and developed a vehicle model with 23 degrees of freedom.

Xu et al. [21] examined the spatial response characteristics and vibration wave propagation mechanisms of a rotating bridge structure under the load of an existing railway train. It was discovered that when the existing railway train was placed on a rotating bridge, the main girder showed a noticeable resonance. König Paul [22,23] proposed a new semi-analytical method for analyzing the dynamic response of railroad bridges under the action of high-speed trains and a dynamic interaction model for the coupled system of railroad bridges, foundations, foundation soils, ballast, track, and high-speed trains, demonstrating the effects of soil–structure interactions, track subsystems, and geometrical defects caused by track irregularities on the dynamic response of example bridges.

Using the “microphone array” method, Moritoh [24] assessed the distribution of structural noise on a concrete bridge on the Shinkansen while moving at a speed of 240 km/h. They also estimated the noise contribution from the far end of the bridge based on the noise data collected underneath the bridge in the field. Wang [25] investigated the effect of different roadbed slabs at a speed of 65 km/h, finding that replacing the rigid roadbed plate with an elastic roadbed slab reduced the noise by 6 dB under A-weighting. Ngai [26] conducted an experiment to examine the specific characteristics of vibration noise radiation in a concrete bridge. The results showed that the vibration and noise energies were primarily concentrated within the frequency range of 20 to 157 Hz when the train was moving at a speed of 140 km/h. Possion [27] performed noise field tests on an underslung steel truss bridge and observed a 6 dB decrease in noise when using A-weighting. It was discovered that while using A-weighting, the noise produced by the train passing over the steel bridge was 10~14 dB louder than the noise produced by the roadbed portion.

Zhang et al. [28,29] conducted an analysis and comparison of the acoustic vibration characteristics and optimal noise reduction mechanism of an overall thickened top plate and a locally thickened top plate on the track of box girder bridges. They discovered that the thickened top plate can effectively decrease the structural noise of the bridges in the high-frequency range. The mechanism was then systematically investigated by using the train–track–bridge spatial coupling dynamics model and the box girder bridge acoustic boundary element model, and it was found that the roof slab was the main noise source of the concrete box girder bridge. Li Xiaozhen and Zhang Xun et al. [30,31] conducted

field vibration and noise radiation law tests on a single- and double-lane simply supported concrete box girder bridge, in which the track type was CRTS III plate ballastless track, there was a high-speed railroad train, and the model was CRH1. The test assessed the acoustic vibration characteristics of the bottom plate in the span of the box girder and found that the concrete bridge produced low-frequency noise. The local stiffness of the box girder plates affected the emission of structural vibration noise. Li Qi et al. [32] conducted an experiment to evaluate the vibration and noise radiation characteristics of a simply supported concrete U-shaped girder bridge. They discovered that when a train traveled over the bridge at a speed of 50–70 km/h, the vibration energy of the bottom plate and web plate of bridge was primarily concentrated in the low-frequency range. When comparing the simply supported box girder bridge to the U-shaped girder, it was observed that the sound pressure level at the bottom measurement point of the U-shaped girder was higher in the frequency range below 200 Hz. Liu et al. [33] assessed the vibration and structural noise of a steel–concrete combination (SCC) box girder in SCC construction using a well-established approach, effectively addressing the gap in knowledge. They also considered the effect of ground reflection in SEA modeling for the first time, using the sound line tracking method.

Liu Quanmin, et al. [34,35] conducted on-site vibration and noise tests on a steel–concrete composite girder bridge with two lines and three spans of continuation and found that the structural vibration noise radiation energy of the steel–concrete composite girder bridge was mainly concentrated at 20~1000 Hz. Du et al. [36] compared the radiated noise of bridges under different train loading conditions by establishing a noise prediction model consisting of a container–train–track–bridge dynamics model, a finite element model, and a boundary element model, revealing the noise radiation mechanism.

In the above numerical simulation of the combined girder bridge, if the computational efficiency of the model can be further improved, it is very beneficial to the study of vehicle–rail–bridge vibration and noise. In this paper, based on the existing vehicle–rail–bridge coupling dynamics research theory, ANSYS 18.0 and MATLAB R2021a are used to study the vibration of the coupled system in the program using a different time-step loading method for the coupled system dynamics calculation. Using the vested vehicle–rail–bridge coupling model, numerical simulation of high-frequency noise in the structure was carried out in VAONE 2021 software, and the noise contributions of different plates to the three field points were obtained, in which the contribution of sound radiation from the top plate was larger than that from the steel structure part.

## 2. Train–Track–Bridge Coupled Vibration Simulation Model

### 2.1. Vehicle Dynamics Model

A train model containing multiple vehicles is established, with 8 vehicle groupings; the motion between each vehicle is independent of each other vehicle, and each vehicle contains 10 degrees of freedom. The vertical model of a single vehicle of the high-speed railroad train analyzed in this paper is shown in Figure 1.

The vehicle parameters in Figure 1 are shown in Table 1.

**Table 1.** Vehicle parameters in Figure 1.

Signs	Meaning
$k_1, k_2$	The spring stiffness in the z-direction for the primary and secondary suspension systems.
$c_1, c_2$	The damping coefficient in the z-direction for the one-system and two-system suspension systems.
$d_1, d_2$	Half of the longitudinal spacing of the one-system and two-system suspensions in the longitudinal direction.
$z_w, z_t, z_c$	The vertical motion of the wheelset, the vertical motion of the bogie, and the vertical motion of the car body.
$\varphi_c, \varphi_t$	The nodding head vibrations of the car body and the bogie.

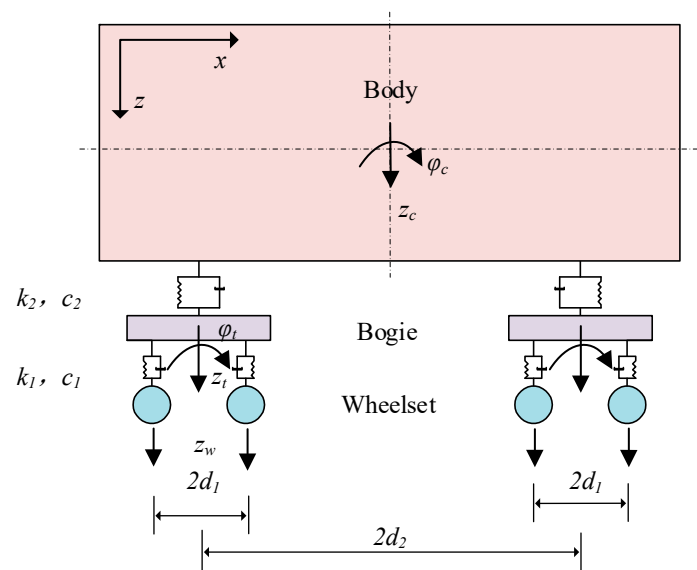


**Figure 1.** Vertical vehicle model.

The vertical static equilibrium position of the vehicle is taken as the initial position to eliminate the effect of gravity. The motion equation of the vehicle is as follows:

$$M_V \ddot{Z}_V + K_V Z_V + C_V \dot{Z}_V = F_V \quad (1)$$

where  $M_V$  represents the mass matrix of the single-section vehicle;  $K_V$  represents the stiffness matrix of the single-section vehicle;  $Z_V$  represents the vertical displacement column matrix of the single-section vehicle; and  $F_V$  represents the vertical wheel–rail force column matrix of the single-section vehicle. The damping matrix  $C_V$  has a similar form to the stiffness matrix  $K_V$ . As a result, it is only necessary to replace the stiffness coefficient  $k$  in  $K_V$  with the damping coefficient  $c$ .

This study focuses on a certain type of rolling stock train. Some of the parameters of the vehicle are shown in Table 2.

**Table 2.** Vehicle parameters.

Vehicle Parameter	Sign	Unit (of Measure)	Value
Distance between front and rear axles	$2d_2$	m	17.5
Distance between bogies	$2d_1$	m	2.5
Rolling circle radius of the wheelset	$R_w$	m	0.46
Wheelset mass	$m_w$	kg	2000
Bogie mass	$m_t$	kg	3200
Body mass	$m_c$	kg	31,600
Vertical damping of primary suspension	$c_1$	N·s/m	25,000
Vertical stiffness of primary suspension	$k_1$	N/m	1,200,000
Vertical damping of secondary suspension	$c_2$	N·s/m	120,000
Vertical stiffness of secondary suspension	$k_2$	N/m	115,000

## 2.2. Track Dynamics Modeling

This paper examines the dynamic characteristics of a specific type of high-speed railroad slab ballastless track; its structure and mechanical vertical model is illustrated in Figure 2. Rails are coupled to the bridge beneath them by fastener forces.  $k_r$  is the vertical stiffness of the fastener and  $c_r$  is the vertical damping of the fastener. A two-node Euler beam unit is used to make the rail model when only the vertical vibration of the rail structure is being considered. Each node has only a vertical bending degree of freedom  $\varphi$  and a vertical degree of freedom  $Z$ . Some of the parameters of the track dynamics structure used are shown in Table 3.

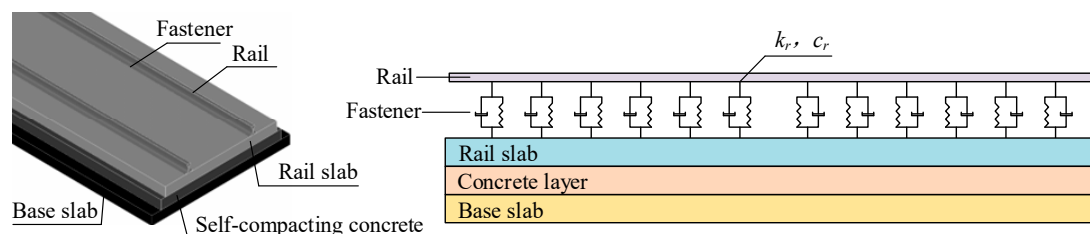


**Figure 2.** Slab ballastless track structure and mechanical vertical model.

**Table 3.** Selected parameters of the track dynamics structure.

Track Component	Parameter	Unit	Value
Rail	Density	kg/m <sup>3</sup>	7860
	Cross-sectional area	m <sup>2</sup>	$7.745 \times 10^{-3}$
	Cross-section moment of inertia	m <sup>4</sup>	$0.3217 \times 10^{-4}$
	Elastic modulus	MPa	$2.059 \times 10^5$
	Element length	m	0.65
Fastener	Vertical stiffness	kN/m	17.5
	Vertical damping	kN·s/m	2.5
Rail slab	Concrete strength grade	/	C60
	Width	m	2.5
	Thickness	m	0.2
Self-compacting concrete	Concrete strength grade	/	C40
	Width	m	2.7
	Thickness	m	0.09
Base slab	Concrete strength grade	/	C40
	Width	m	3.1
	Thickness	m	0.2

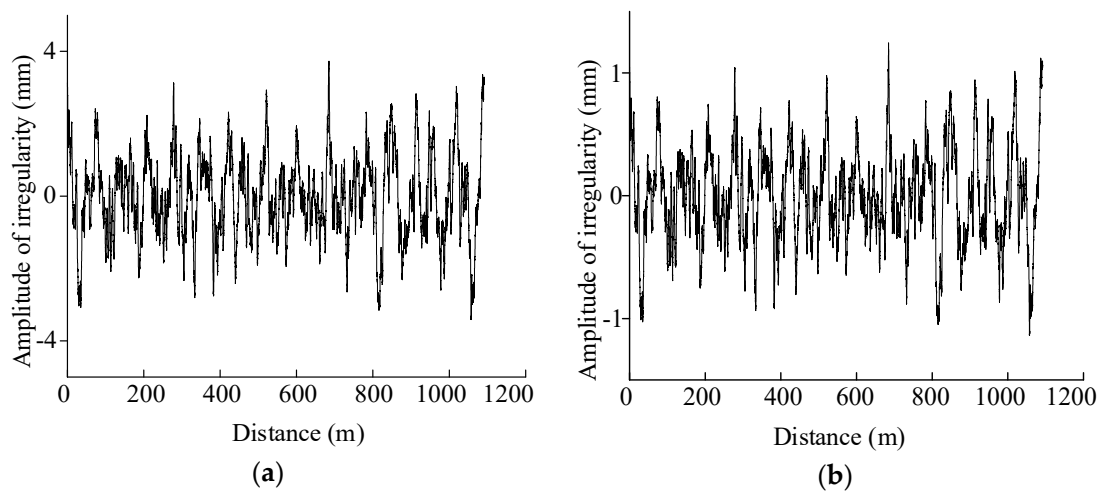
## 2.3. Bridge Finite Element Model

This paper focuses on studying a steel–concrete composite beam without ballast, specifically designed for high-speed railway bridges with a span of 48 m and a speed of 350 km/h. The cross-section of the bridge adopts a single-box single-chamber combination cross-section, which consists of a concrete deck slab and a grooved steel box. The steel girder features a single-box, single-compartment channelized cross-section that is encompassed by the bottom plate, the top plate of the upper flange, and the web plate. Longitudinal strengthening ribs are installed on both the bottom plate and the web plate of the bridge. The bridge has a height of 4.005 m and a span of 48.6 m. The concrete deck plate section consists of a top plate with a width of 12.6 m. The concrete at the flange of the top plate has a thickness of 0.22 m, while the concrete at the peg connection is 0.55 m thick. The concrete at the middle of the span has a thickness of 0.3 m. The slotted steel box girder portion has an upper flange with a width of 1 m and a thickness of 0.032 m. The web plate has a height of 3.45 m and a thickness of 0.016 m. The entire bridge is constructed using Q370qE steel



**Table 5.** Table of ballastless track irregularity of high-speed railway in China.

Irregularity Type	The First Section			The Second Section			The Third Section			The Fourth Section		
	$f$	$A$	$k$	$f$	$A$	$k$	$f$	$A$	$k$	$f$	$A$	$k$
Rail gauge irregularity	0.109	$5.4 \times 10^{-2}$	0.83	0.2938	$5.1 \times 10^{-3}$	1.90	0.5	$1.9 \times 10^{-4}$	4.59	/	/	/
Horizontal irregularity	0.0258	$3.6 \times 10^{-3}$	1.73	0.1163	$4.4 \times 10^{-2}$	1.05	0.5	$4.6 \times 10^{-3}$	2.09	/	/	/
Alignment irregularity	0.045	$4.0 \times 10^{-3}$	1.87	0.1234	$1.1 \times 10^{-2}$	1.54	0.5	$7.6 \times 10^{-4}$	2.82	/	/	/
Height irregularity	0.0187	$1.1 \times 10^{-5}$	3.39	0.0474	$3.6 \times 10^{-3}$	1.93	0.1533	$2.0 \times 10^{-2}$	1.36	0.5	$4.0 \times 10^{-4}$	3.45

**Figure 4.** Spatial samples of left and right rail height irregularity. (a) Spatial samples of left rail height irregularity. (b) Spatial samples of right rail height irregularity.

### 2.5. Establishment and Solution of Vehicle–Track–Bridge System Equations

Based on the bridge, vehicle, and track dynamics models developed in this section, and the wheel–rail interaction simulated by the Hertz nonlinear contact model, the dynamics equations of the entire coupled system in this section can be obtained as shown in the following equation:

$$\begin{cases} M_B \ddot{Z}_B + K_B Z_B + C_B \dot{Z}_B = F_B \\ M_V \ddot{Z}_V + K_V Z_V + C_V \dot{Z}_V = F_V \\ M_R \ddot{Z}_R + K_R Z_R + C_R \dot{Z}_R = F_R \end{cases} \quad (3)$$

where  $C$ ,  $K$ , and  $M$  represent the system damping, stiffness, and mass matrices, respectively.  $Z$  is the generalized displacement vector of the system, and the subscripts  $B$ ,  $V$ , and  $R$  represent the bridge system, the vehicle system, and the rail system, respectively.  $F$  is the external load vector of the system.

For the vehicle system, the external load vector is the vertical wheel–rail force. For the rail system, the external load vector is the vertical wheel–rail force and the support force provided by the bridge through the fasteners, and for the bridge system, the external load vector is the vertical force exerted on the bridge by the rail through the fasteners. For finite element structures such as bridges and track plates, the complete transient response analysis is solved by the Newmark integration method that comes with ANSYS. The vehicle–rail system employs the MATLAB-programmed Newmark integration method to solve the problem.

### 3. Analysis of Vehicle–Track–Bridge Coupled Vibration Model Simulation Results

The program described in this document can replicate the dynamic behavior of vehicle–track–bridge systems during the passage of a train over a bridge, specifically focusing on various parameters such as the vertical forces acting on the wheel and rail, the vertical deflection of the bridge structure, acceleration, and the internal forces within the bridge structure. The program sets up the train vehicle model and the rail model in MATLAB and invokes the Apdl program to create the finite element model of rail plates, self-compacting concrete layers, and other rail structures, such as the bridge finite element model and the rail plate structure model. The contact action point between the rail and the finite element model is determined by the geometric position of rail fasteners. The displacement and interaction force of the contact point are considered as the key parameters. These parameters are transferred within the time step to enable the joint simulation and analysis of the upper vehicle–track system and the lower finite element system. The dynamic model of the train–rail–bridge is illustrated in Figure 5. Figure 6 illustrates the structure for calculating the program.

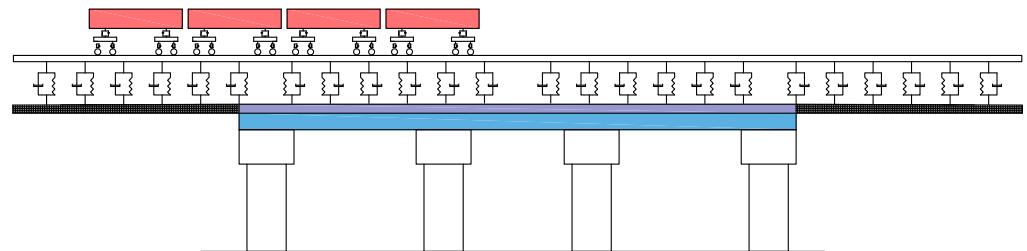


Figure 5. Train–track–bridge dynamics model.

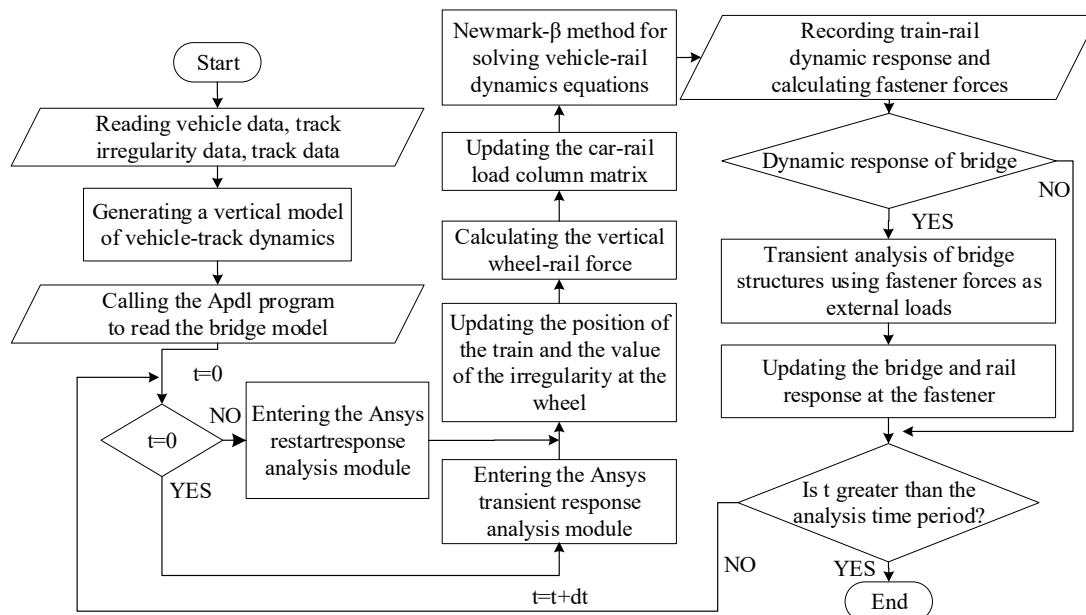


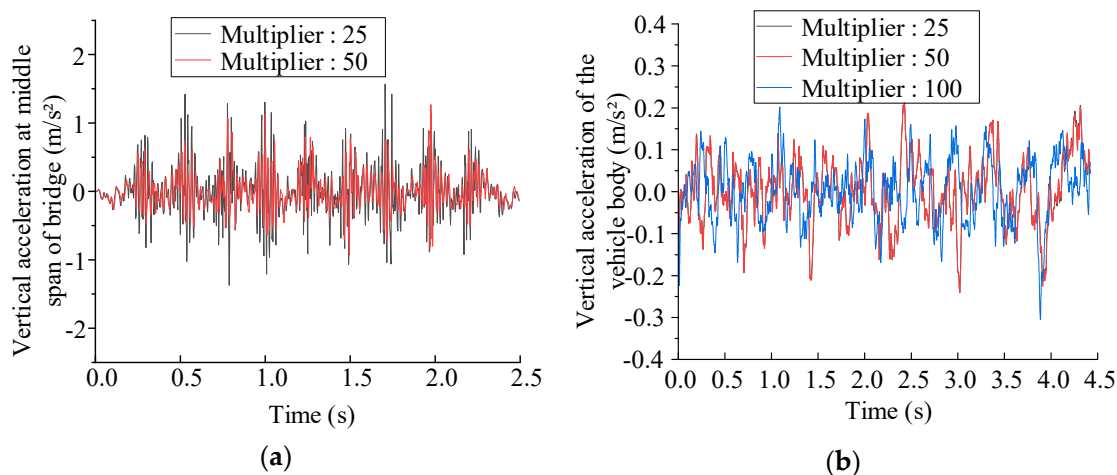
Figure 6. Flow chart of vehicle–rail–bridge coupling calculation.

#### 3.1. Analysis Methods Considering Different Time Stepping Loading

In the process of structural transient dynamic analysis, choosing the proper time integration stepping determines the running time of the model and the accuracy of the correctness and convergence effect of the solved problem. For general problems, decreasing the integration time stepping leads to increased accuracy in calculation results but requires a higher computer hardware configuration and greater power consumption. Conversely, increasing the integration time stepping will inevitably compromise the accuracy of higher-

order response simulation. Hence, based on the specific attributes of the problem addressed in this paper, the time stepping for transient analysis is determined by taking into account two factors: (1) the correlation between the time stepping and the highest frequency of the structure response; (2) the correlation between the integration time stepping, grid size, and traveling speed.

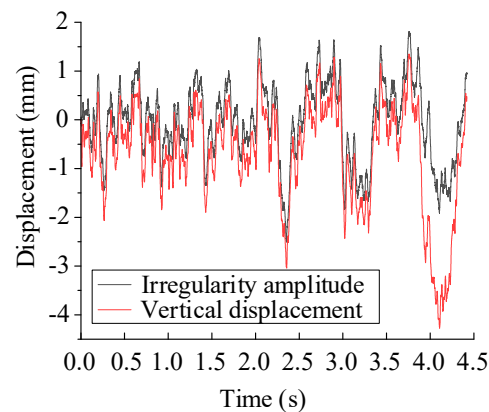
Different time stepping loading multiplicity has a significant effect on the computational efficiency. If equal time stepping is used to calculate the model in this paper, it is expected that the single model calculation time could be up to 8 days, whereas if the 50-fold different time stepping calculation method proposed in this paper is used, the calculation time can be reduced to 4 h. Define the different time stepping loading multiplier as the ratio of the analysis time step of the rail system to the transient analysis time step of the bridge in the finite element software. It can be concluded from the time step in Figure 7 that the smaller the loading multiplier of different time steps, the more accurate the simulation results of the high-frequency band response and the more accurately they reflect the full-band information of the data. The spectrogram analysis reveals that variation in the time stepping loading multiplier has minimal impact on the presentation of the results within a 100 Hz range. Based on this, this paper can realize the method of using the different time stepping method to analyze the results of the dynamics within 100 Hz under the condition of satisfying the accuracy of the resultant data within 100 Hz, which effectively saves computational resources.



**Figure 7.** Results chart for different time stepping loading. (a) Time history of acceleration at midspan of beam. (b) Time history of vehicle acceleration. Note: Multiplier in the diagram represents multiplier for every different time stepping loading.

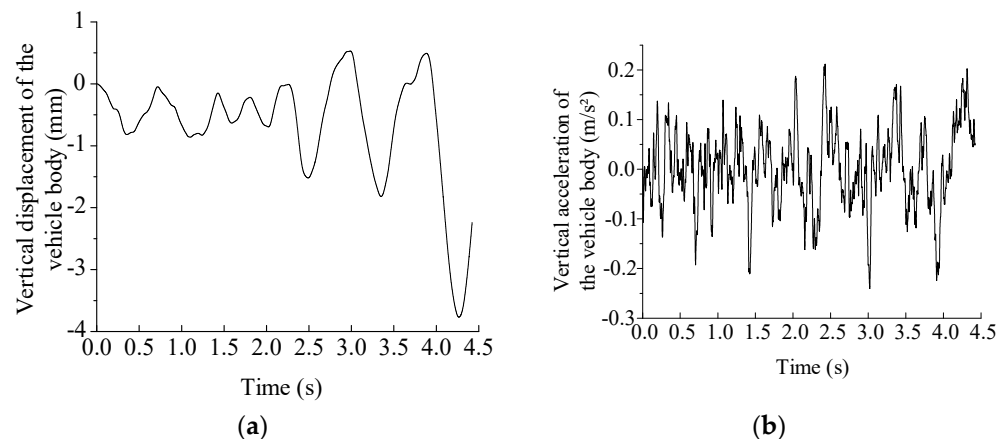
### 3.2. Analysis of Time-Domain Results

The vertical wheel–rail relationship utilized is based on the nonlinear Hertz theory. However, by comparing the time history curve of the vertical displacement of the wheel pair with the curve of the irregularity value of its position, the following law may still be derived: Within the time frame of 0 to 3.5 s, the wheel set has not yet reached the bridge. At this level, the general principle holds true, stating that the displacement of the wheel set is equal to the combined value of the irregularity amplitude, bridge displacement, and rail displacement. Currently, the patterns and magnitudes of the two situations in Figure 8 are approximately equal. The irregularity excitation is the causal factor, while the vertical displacement of the wheel set is the consequent outcome. The abrupt variation in the magnitude of irregularity at a certain moment should be evident in the chronological record of the vertical displacement of the wheel set. After a duration of 3.5 s, the vertical displacement of the wheel pair exceeds the amplitude of the irregularity at this location, reaching a magnitude of 3.5 mm, as a result of the bridge displacement. This observation is consistent with the fundamental principle.



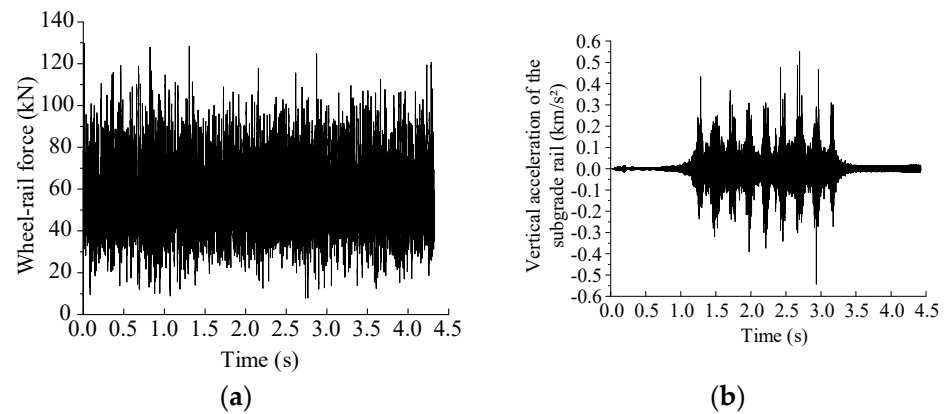
**Figure 8.** Time history of vertical displacement of the first wheel set of the train.

By analyzing the vertical displacement and vertical acceleration curves of the vehicle body, it is evident that the vertical displacement time history curve of the vehicle body remains relatively stable, ensuring a comfortable passenger experience. Additionally, based on Figure 9, it is difficult to precisely determine the exact time when the train crosses the bridge. However, it is apparent that the bridge structure does not have a significant impact on the dynamic performance parameters of the vehicle. The vertical acceleration of the vehicle body fluctuates between  $-0.2$  and  $0.2$   $\text{m/s}^2$ , which is far less than the  $1.3$   $\text{m/s}^2$  specified in the standard, demonstrating the accuracy of the simulation.



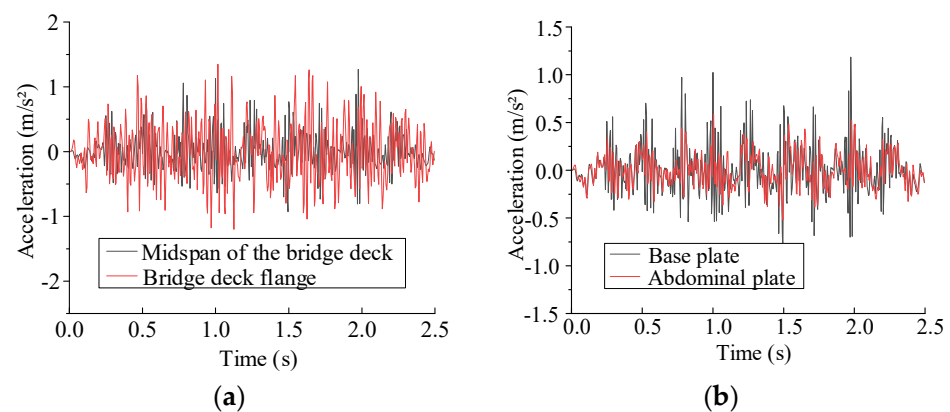
**Figure 9.** Vertical dynamic response of the train body. (a) Time history of vertical displacement of the vehicle body. (b) Time history of vertical acceleration of the vehicle body.

Figure 10a illustrates a dense curve representing the time history of the wheel–rail force. This curve specifically shows the contact force between a single wheel on the wheel set and the rail, rather than the overall contact force between the entire wheel set and the rail. The curve typically exhibits fluctuations around  $56$   $\text{kN}$ , which is directly correlated to the static wheel weight of the wheel. The range of fluctuation, which spans from  $-50$  to  $50$   $\text{kN}$ , indicates the medium- and high-frequency characteristics of the axle coupling issue examined in this study. The rail vibrates with high frequency and clear periodic characteristics due to the direct influence of this high-frequency excitation force. In Figure 10b, the rail node can experience a peak acceleration of up to  $500$   $\text{m/s}^2$ .



**Figure 10.** Time history of vertical acceleration of the rail. (a) Vertical wheel–rail force. (b) Vertical acceleration of the rail.

The time history curve of the bridge indicates that the vibration amplitude of the bridge deck flange is considerably higher than that at the midspan. This difference can be attributed to the thickness of the plate and the distance from the excitation site. The model train load is a load that only acts in one direction, and the flange of the bridge deck is positioned closer to the loading point. The bottom plate of the steel structure exhibits a higher vibration intensity compared to the web, offering a valuable indication for investigating methods to reduce vibration and noise in this particular type of bridge. The displacement curves of the different components of the concrete structure nearly coincide, but it is still evident that the vertical displacement of the upper component exceeds that of the lower component, indicating damping and vibration isolation properties of the concrete structure. Time history of the dynamic response of the bridge structure are shown in Figure 11.



**Figure 11.** Time history of the dynamic response of the bridge structure. (a) Acceleration diagram of the bridge deck flange and midspan. (b) Comparison of acceleration of steel base plate and abdominal plate.

#### 4. Prediction Model for High-Speed Railway Composite Steel–Concrete Beams with High Noise

##### 4.1. Structural Acoustic Radiation Theory Based on Statistical Energy Analysis Method

Conventional analysis techniques, such as finite element modeling, are employed to examine the dynamic characteristics of bridge structures. The outcomes of dynamic simulations solely encompass low-frequency data, whereas the dynamic behavior of the structure in the middle- and high-frequency data ranges is absent. The boundary element method, akin to the theory of finite element analysis, presents challenges in solving high-frequency, high-modal-density problems. Statistical energy analysis (SEA) is highly efficient in resolving dynamic problems with high frequency and high modal density.

In the context of a complex system involving the dynamics of vehicles, tracks, and bridges, the SEA model is employed. This model incorporates a plate analysis model to study the structure of the bridge. The external excitation force acting on the bridge deck, which carries information about the frequency range being analyzed, is utilized as the input energy for the system and subsequently resolved. The equation governing the balance of power flow in the established system is as follows:

$$\omega \begin{bmatrix} \eta_1 + \sum_{i \neq 1}^N \eta_{1i} & -\eta_{12} & \cdots & -\eta_{1N} \\ -\eta_{21} & \eta_2 + \sum_{i \neq 2}^N \eta_{2i} & \cdots & -\eta_{2N} \\ \vdots & \vdots & \ddots & \vdots \\ -\eta_{N1} & \cdots & \cdots & \eta_N + \sum_{i \neq N}^N \eta_{Ni} \end{bmatrix} \begin{bmatrix} E_1 \\ \vdots \\ E_k \\ E_{k+1} \\ \vdots \\ E_N \end{bmatrix} = \begin{bmatrix} P_1 \\ \vdots \\ P_k \\ 0 \\ \vdots \\ 0 \end{bmatrix} \quad (4)$$

where  $\omega$  represents the natural frequency,  $\eta_i$  the internal loss factor of subsystem  $i$ ,  $\eta_{ij}$  and  $\eta_{ji}$  the coupling loss factors between subsystems, and  $E_i$  and  $E_j$  the energies of subsystems  $i$  and  $j$ , respectively.

The bridge deck subsystem is the first in the  $k$ th order and is the energy input to the bridge deck subsystem from the under-track excitation force. The remaining subsystems are the steel structure part of the composite beam and the bridge deck subsystem, which is not directly affected by the train load. The corresponding input energy is zero. By solving this set of equations, the average energy stored in each subsystem can be solved, and the average square vibration velocity of the subsystem can be obtained.

Plate noise contribution: The sound pressure generated by each individual plate of the bridge structure at the site can be analyzed by comparing the noise contribution of the plate to the overall noise produced by the entire structure. The noise generated by the steel box composite beam structure is generally attributed to three types of plates: the top plate, bottom plate, and abdomen plate. The contribution of plates such as diaphragms and stiffeners is quite insignificant. The noise generated by a certain plate at a specific frequency at a specific place in an acoustic field can be mathematically represented by the following formula:

$$\eta_i = \frac{P_{1,i}^2}{P_i^2} = \frac{10^{0.1Lp_{1,i}}}{10^{0.1Lp_i}} \quad (5)$$

where  $\eta_i$  represents the structural noise contribution of a panel at frequency  $i$ ,  $Lp_{1,i}$  and  $p_{1,i}$  denote the sound pressure level and sound pressure generated by a panel at the measurement point at frequency  $i$ , respectively, and  $Lp_i$  and  $p_i$  represent the total sound pressure level and total sound pressure generated by all panels at the measurement point at frequency  $i$ .

The modal density is an indicator of the capacity of the system to store energy. This work focuses on analyzing the problem of noise radiation from bridges. In this context, the majority of structures may be simplified as plate structures. Mathematical methods can be used to determine the modal density of these simplified substructures. The expression for the modal density of a vibrating plate is as follows:

$$n(f) = \frac{S\sqrt{12}}{2c_B t} \quad (6)$$

where  $c_B$  represents the bending wave velocity,  $S$  represents the area of the plate, and  $t$  the thickness of the plate.

The internal loss factor  $\eta_i$  is defined as the ratio of the energy lost per unit time to the average stored energy during the vibration cycle of a subsystem. It is generally accepted that for any subsystem the damping of the system is usually determined by no more than

three damping mechanisms. The internal loss factor of a structural subsystem can be expressed as

$$\eta_i = \eta_{is} + \eta_{ir} + \eta_{ib} \quad (7)$$

where  $\eta_{ib}$  represents the damping of the boundary connection of the structural subsystem.  $\eta_{is}$  is the damping caused by friction within the structural subsystem, and  $\eta_{ir}$  is the damping of the vibration sound radiation of the structural subsystem.

In this paper, the internal loss factor of the concrete structure is taken as 1.5%, and the internal loss factor of the steel structure is taken as 0.1%.

The coupling loss factor  $\eta_{ij}$  is defined as the transmission loss of energy at the connection between two coupled subsystems  $i$  and  $j$ . The coupling loss factor used in this paper is calculated as follows:

$$\eta_{12} = \frac{lC_g}{\pi\omega A_1} \tau_{12} \quad (8)$$

where the wave propagation coefficient from structure 1 to structure 2 is denoted by  $\tau_{12}$ . The length of the line connection is represented by  $l$ .  $C_g$  represents the group velocity,  $A_1$  represents the surface area of substructure 1, and  $\omega$  represents the center frequency of the frequency band.

The technical route of the statistical energy method is shown in Figure 12.

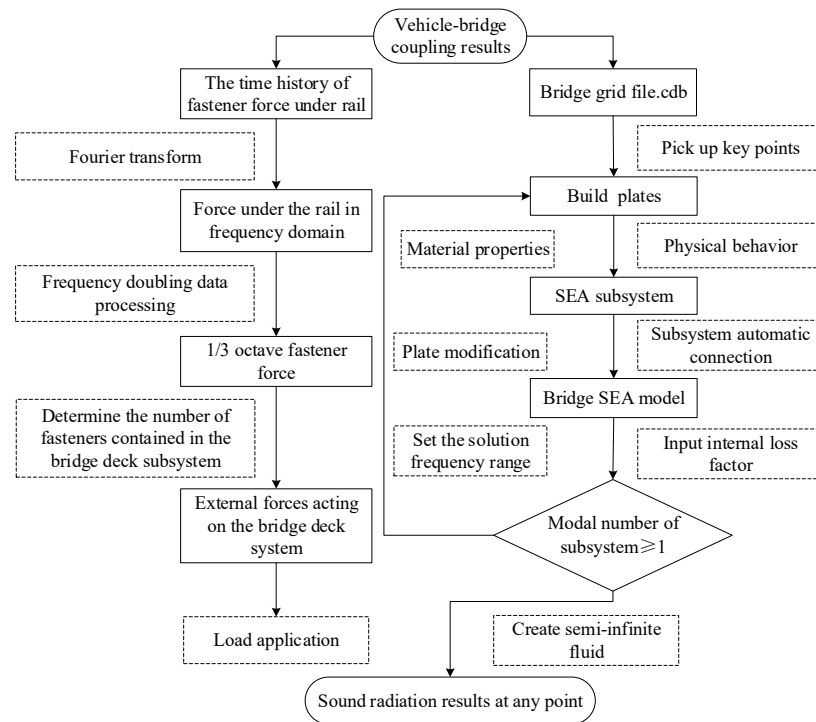


**Figure 12.** Technology roadmap for statistical energy methods.

#### 4.2. Determination of External Excitation Forces for Bridge Deck Systems

To determine the properties of the force that the rail applies to the bridge, we retrieved the time history data of the force exerted by each individual rail fastener. We then conducted fast Fourier transformation and octave data processing. The results are displayed in Figure 13 below. The time history of the fastener force demonstrates that it can reach a maximum value of 40 kN, exhibiting a distinct periodic pattern. The spectrum diagram indicates that the fastener force reaches a maximum value of 5.5 kN at a frequency of 10 Hz. Additionally, the octave diagram reveals that the fastener force continues to exhibit data distribution beyond 1000 Hz, highlighting the medium- and high-frequency features of the force.

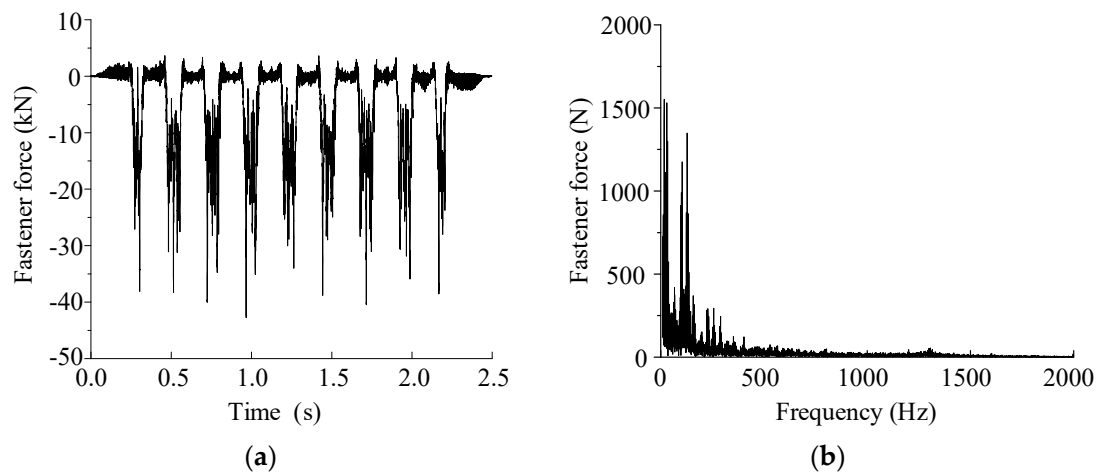


**Figure 13.** Fastener force time history and frequency data results. (a) Time history of fastener force. (b) Spectrum of fastener forces.

At the same time, combining the frequency bands analyzed in this section, the spectral data of 100~1000 Hz is extracted for the solution of the excitation force outside the bridge deck. The original fastener force data are filtered at 100 Hz, and a Fourier inverse transformation is performed to obtain the filtered time history curve of the under-track force, as shown in Figure 14. It can be seen that the excitation force applied by the steel rail to the bridge has a clear periodic pattern.

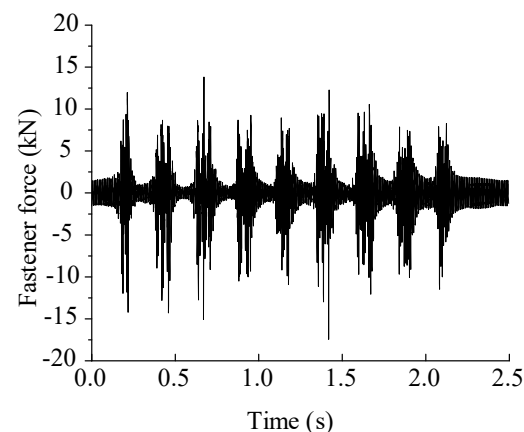


**Figure 14.** Time-domain diagram of fastener force after high-pass filtering.

The bridge deck in the model has a longitudinal length of 4 m, and the fasteners are spaced longitudinally at intervals of 0.65 m. Given that the fasteners are evenly distributed on the center line of the track, there are a total of 12 fasteners on one bridge deck. The force exerted by the train load on the rail is transmitted to the bridge through the square root of the sum of the squares of the forces of each supporting spring. Refer to the formula for the precise calculation procedure:

$$F_b = \sqrt{\sum_{n=1}^M |f_n|^2} \quad (9)$$

where  $F_b$  represents the external force acting on the bridge deck system,  $M$  denotes the number of fasteners on the bridge deck, and  $f_n$  represents the force acting on the bridge deck system due to the spring force of the  $n$ th fastener.

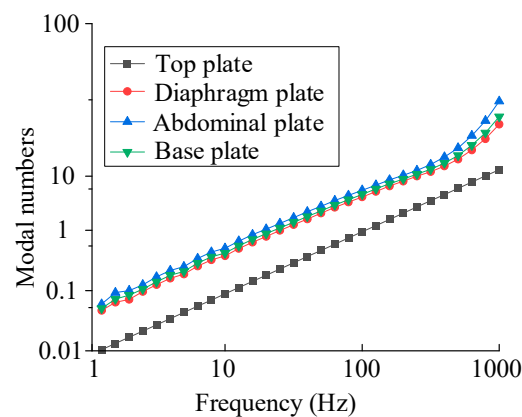
The forces of the fasteners and the external excitation force spectrum of the bridge deck within the scope of the statistical energy model analysis are shown in Table 6.

**Table 6.** Data table for external excitation force of bridge deck.

Frequency (Hz)	Excitation Force (N)	Frequency (Hz)	Excitation Force (N)
100	1385	400	415
125	1212	500	381
160	1039	630	346
200	866	800	381
250	692	1000	277
315	623		

#### 4.3. Simulation Results of Medium- and High-Frequency Noise

The steel–concrete composite beam mentioned previously served as the subject of study for the development of a statistical energy analysis model. The model has a total length of 48 m. Typically, the concrete top plate has a thickness of 0.35 mm, whereas each steel plate has a thickness of 2 mm. The model comprises a grand total of 98 plate subsystems, consisting of 24 bridge deck plate subsystems, 24 abdominal plate subsystems, 24 bottom plate subsystems, and 26 diaphragm plate subsystems. The steel plate subsystem has an internal loss factor of 0.1%, whereas the concrete plate has an internal loss factor of 1.5%. Figure 15 displays the quantity of bending modes for each subsystem. When the frequency of analysis exceeds 100 Hz, the subsystem exhibits more than one mode, thereby satisfying the criteria of statistical energy analysis. Hence, the frequency range employed for analyzing medium- and high-frequency noise radiation is 100–1000 Hz.

**Figure 15.** The modal number of bending modes of steel–concrete composite beam subsystem.

In order to consider the radiation noise capacity of the bridge structure, three semi-infinite fluid subsystems are established in the model to receive the sound pressure radiated by each subsystem of the bridge. The locations of the semi-infinite fluid subsystems in relation to the steel box composite beam segments are indicated by the field points A, B, and C in Figure 16. Detailed locations of field points A, B, C are shown in Figure 17. The semi-infinite fluid can exhibit the sound pressure radiation of the interconnected plates. By modifying the kind and quantity of the linked plates, one can determine the sound radiation values of various plates at the designated location and resolve the sound contribution of each individual plate.

The radiation efficiency, or radiation ratio, is the quotient of the sound power radiated by a structure to the sound power radiated by a huge rigid piston with equivalent surface area and root mean square velocity. As shown in Figure 18, for a plate structure with finite dimensions, the radiation efficiency approaches 1 when the frequency exceeds the critical frequency. Below 500 Hz, the concrete roof has a much higher radiation efficiency compared to the steel plate. Beyond a frequency of 500 Hz, the steel structure has a higher radiation efficiency compared to the concrete roof, and this efficiency is somewhat above

1. The A and B field points are situated in close proximity to the top and bottom plates of the bridge, respectively, and are closer to the sound source compared to the C field point. As a result, the radiation sound pressure level is considerably higher than the sound pressure level at the C field point. The sound pressure level experiences a sudden increase at frequencies of 100 Hz and 1000 Hz, which corresponds to the frequency-dependent variation in the external force that excites the bridge. This force mainly distributes energy in the low-frequency range. At point A, the highest value of 88 dB is seen at a frequency of 100 Hz. All three data points within each frequency range have values exceeding 65 dB. At the upper limit of the frequency range being examined, specifically at 1000 Hz, there is an abrupt transition, suggesting that the anticipated noise level at this particular moment is not accurate.

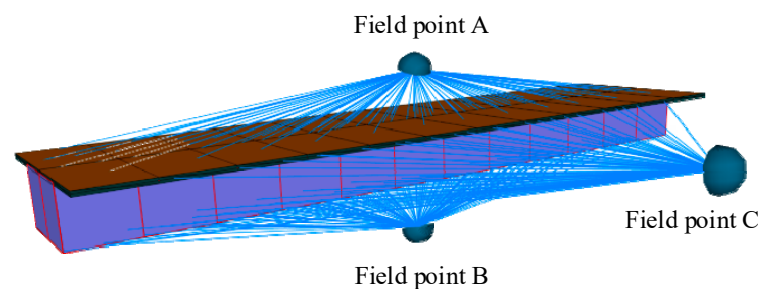


**Figure 16.** Semi-infinite fluid subsystem. (The brown portion represents concrete and the purple portion represents steel.)

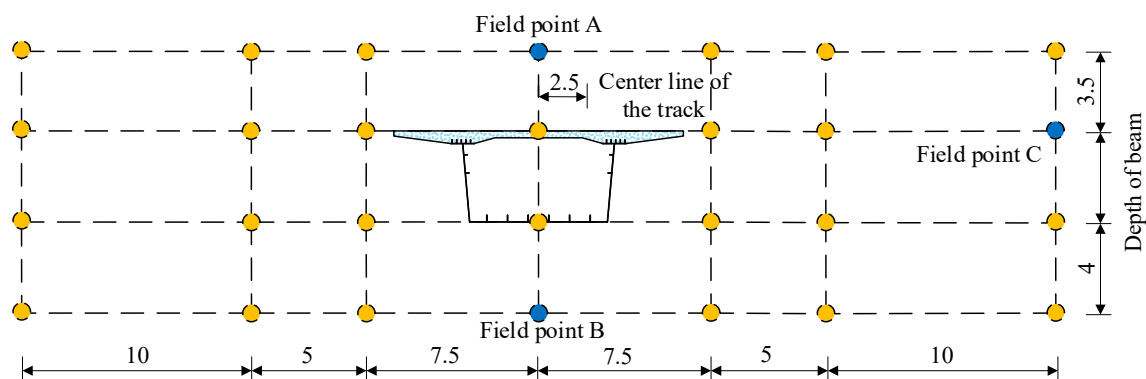
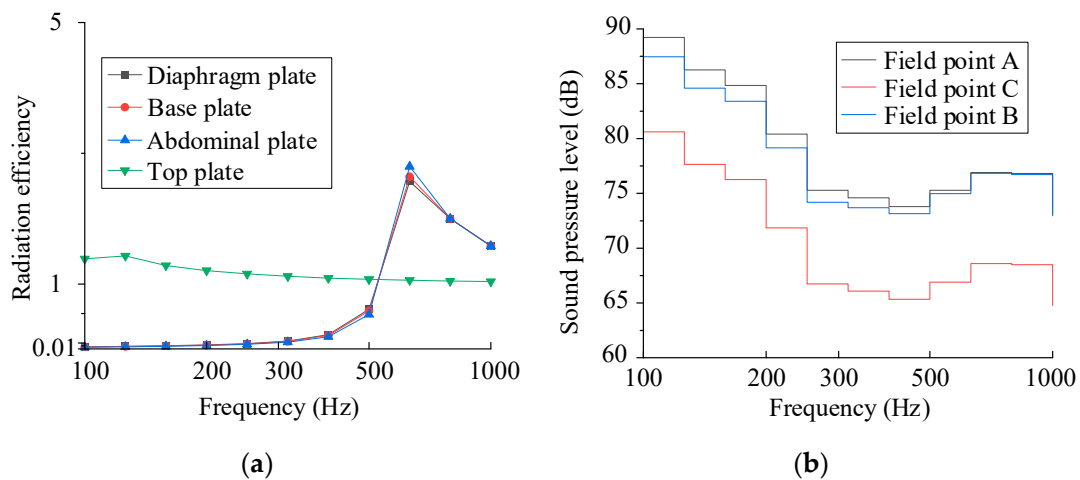


**Figure 17.** Acoustic field point diagram (m).

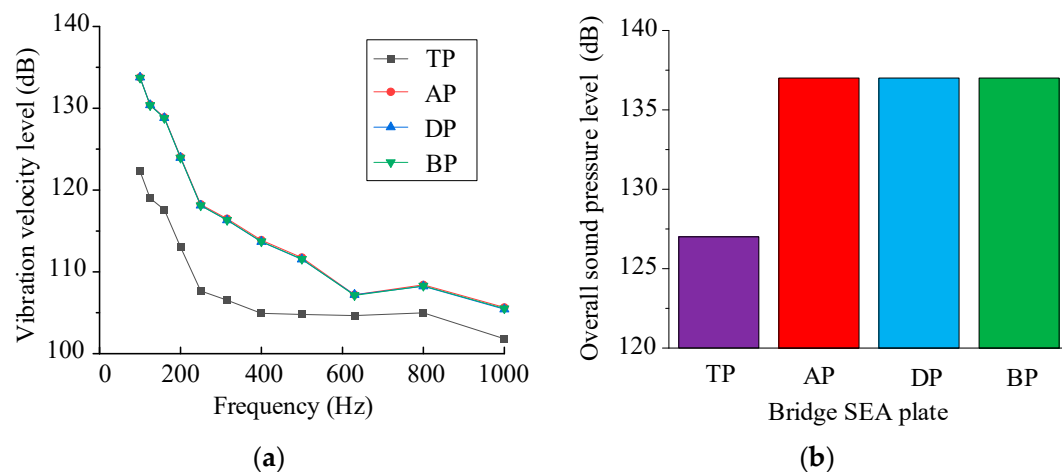
The vibration velocity data for each plate of the bridge was extracted, as depicted in Figure 19. The concrete plate has a significantly lower average vibration velocity compared to the steel construction. The concrete plate exhibits a total vibration level of 127 dB, while the steel plates demonstrate a comparable vibration level due to their identical thickness, similar size, and direct loading without any additional load. The mean overall vibration level is approximately 138 dB.

Figure 20 illustrates the respective impact of various components of the bridge structure on the emission of noise at three specific acoustic locations, namely, points A, B, and C. Point A is situated at the highest point of the bridge structure. The findings indicate that the floor plate has minimal impact on this particular spot across the whole frequency range. The concrete roof plate significantly contributes to the noise at this location, with a noise level of up to 92 dB. Point B is situated near the base of the bridge structure. The floor plate contributes more to this point compared to point A. At lower frequencies, the concrete roof is primarily responsible for the noise emitted at this location. However, around 250 Hz the steel structure becomes more efficient at radiating noise and its contribution surpasses that of the concrete component. In general, the concrete structure has the greatest impact on this aspect, whereas the contribution of the steel structure is comparable. The concrete

roof has a greater impact on the noise at the C site in the lower frequency range. However, at 500 Hz, the noise contribution from the concrete slab reduces due to reduced radiation efficiency. At this point, the steel web, stiff floor, and diaphragm plate become more significant contributors to the noise at the C site. By examining the histogram of the total sound pressure level contribution, it is evident that the concrete slab carries the train load directly, resulting in its significant contribution to the overall sound pressure level at the C site. The primary contributors to the noise at the C field point of the bridge are the bottom plate and the abdominal plate made of steel. Therefore, it is imperative to conduct comprehensive study on the vibration and noise reduction capabilities of these two plates.



**Figure 18.** Simulation results of point noise radiation in medium- and high-frequency fields. (a) Radiation efficiency of each subsystem of bridge. (b) Radiation spectrum curve of medium- and high-frequency field point noise.



**Figure 19.** Vibration simulation results of medium- and high-frequency plates. (a) Vibration velocity of medium- and high-frequency bridge plate. (b) The total vibration level of medium- and high-frequency bridge plate. Notes: TP, AP, DP, and BP represent top plate, abdominal plate, diaphragm plate, and base plate, respectively.

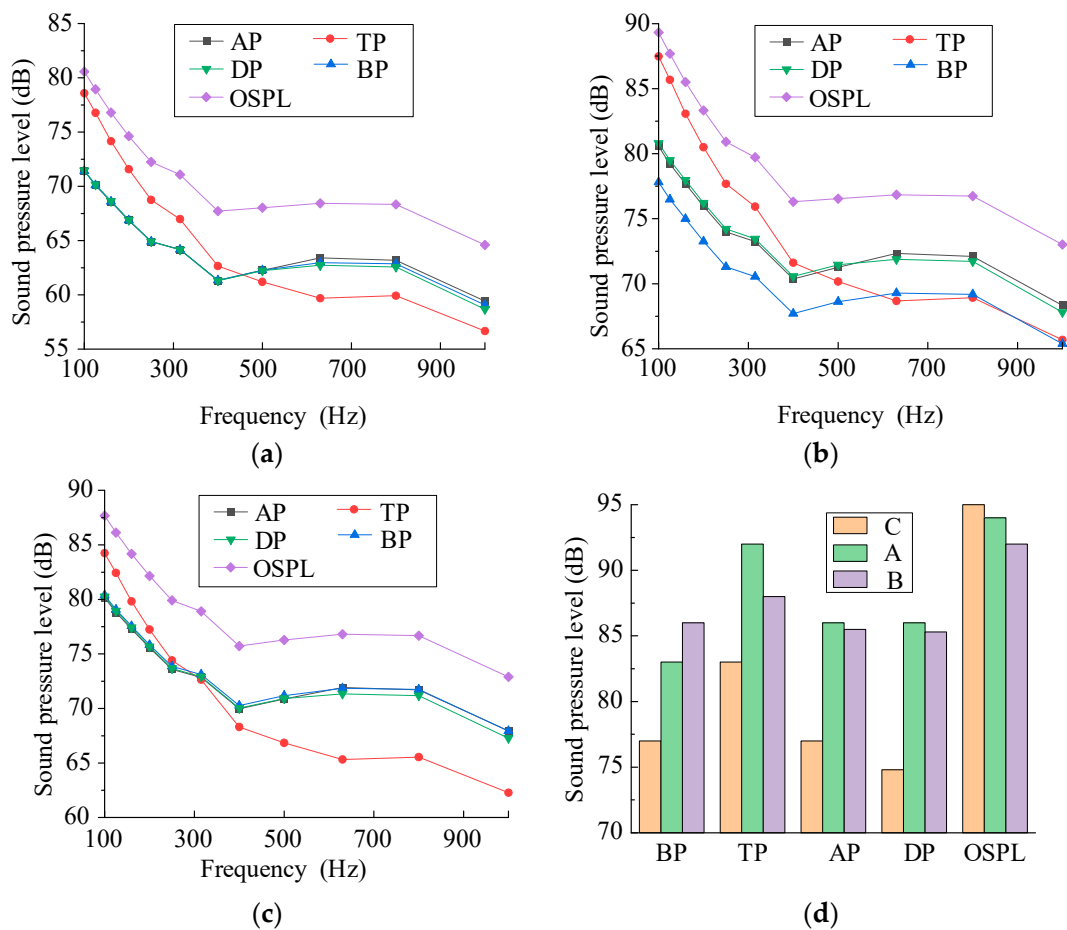


**Figure 20.** Results of the contribution of the high-frequency bridge plate in three field points A, B, and C. (a) The contribution spectrum of high-frequency bridge plate in field point A. (b) The contribution spectrum of high-frequency bridge plate in field point B. (c) The contribution spectrum of high-frequency bridge plate in field point C. (d) Bar chart of the total sound pressure level contributed by the panels at the three points. Notes: TP, AP, DP, BP, and OSPL represent top plate, abdominal plate, diaphragm plate, base plate, and overall sound pressure level, respectively.

Regarding the contribution of the bridge base plate, bridge top plate, and bridge abdominal plate to the mid–high-frequency noise radiation at the A, B, and C field points, the calculation results are shown in Figure 21. According to the data, the base plate has the most contribution to the B field point compared to the other two acoustic field points, accounting for 24% of the noise. The abdominal plate also contributes a similar proportion of noise to all three field points, with an average contribution rate of 17%. Among all three locations, the concrete deck plate has the highest contribution rate, with rates of 61%, 56%, and 36% for sites A, B, and C, respectively. There is an urgent need to study the vibration and noise reduction in concrete bridge decks.

The following sites were established in the software to obtain the total sound pressure level distribution of the medium- and high-frequency noise radiation at the point: The structural spatial radiation noise is symmetrically distributed along the center line of the bridge when subjected to a unidirectional traffic load. The sound pressure level of the structure noise is lower on the outside of the bottom plate and abdominal plate compared to above the top plate. The radiation noise of the bridge structure demonstrates the properties of cylindrical propagation in the far region, with a lower rate of attenuation in the far field compared to the near field. Overall sound pressure level at medium- and high-frequency field points is shown in Figure 22.

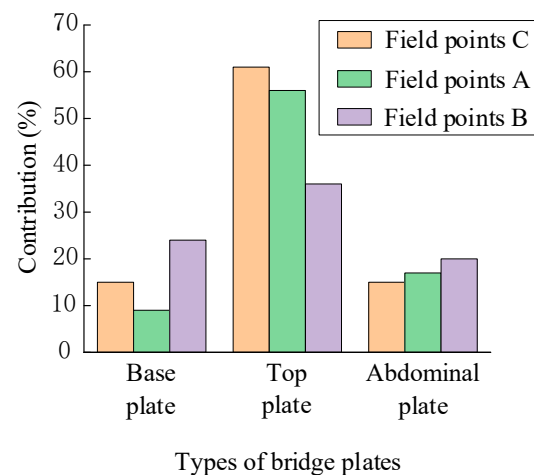


**Figure 21.** Noise contribution of the plate at the medium-high-frequency field point.

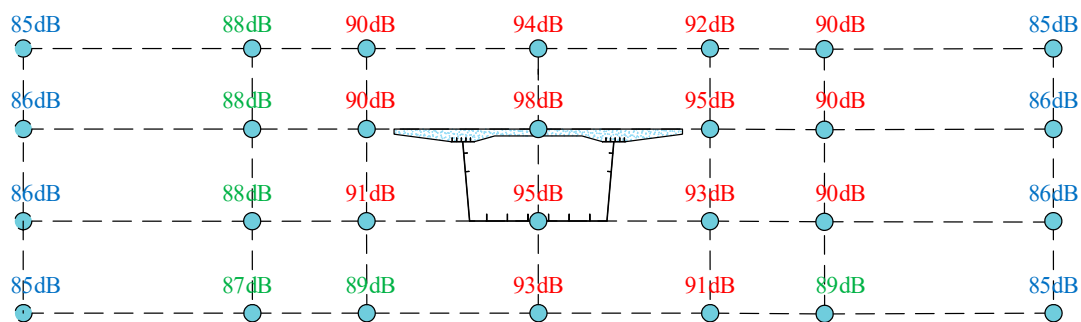


**Figure 22.** Overall sound pressure level at medium- and high-frequency field points.

## 5. Conclusions

This paper examines the vibration and noise radiation characteristics of high-speed railway steel-concrete composite box girder bridges. The investigation is conducted in detail, considering both the theoretical background and numerical simulation. The scientific findings and legislation can be summarized as follows:

- (1) By employing a time stepping ratio of 50, it is possible to conduct a coupled analysis of vehicle-track-bridge vibrations. This approach effectively enhances calculation efficiency and reduces the size of result files, while maintaining the results' accuracy within a range of 100 Hz.
- (2) The results of the simulation indicate that the concrete roof bears the direct load from the train and is the primary source of noise radiation at each acoustic field point, particularly for medium- and high-frequency noise. The concrete roof in this study contributes significantly, with an average contribution of 50%, to the three acoustic field points. Comparing the noise radiation efficiency of concrete and steel structures reveals that in the medium-frequency range the concrete slab has a higher sound radiation efficiency than the steel structure slab. However, in the high-frequency range the steel structure has a higher sound radiation efficiency than the concrete slab.

In addition to the above conclusions, the following issues require further research in the future: The vibration response of the real bridge needs to be measured for further validation of the self-programmed vehicle-rail-bridge program in this paper. The vehicle-rail-bridge coupling model established in this paper does not take into account the influence of wheel-rail creep-slip force on the results; there is also a need to expand the degrees of freedom of the rail unit used and to consider the lateral vibration of each part of the vehicle as a degree of freedom. As the number of degrees of freedom increases, it may

become challenging to find a suitable multiplier for different time-step loading to improve computational efficiency.

**Author Contributions:** Conceptualization, J.S., L.Z. and W.M.; data curation, W.M.; methodology, J.S., L.Z. and W.M.; software, W.M., L.Z. and H.N.; validation, J.S. and B.M.; visualization, B.M., H.D. and G.Z.; writing—original draft, J.S. and L.Z.; writing—review and editing, J.S. and L.Z. All authors have read and agreed to the published version of the manuscript.

**Funding:** The research was financially supported by the Eighth National “Ten Thousand Talents Plan for Top Young Talents” and the National Natural Science Foundation of China (52378120).

**Data Availability Statement:** The data provided in this study could be released upon reasonable request. The authors state that all data, models, and code generated or used during this study are available from the corresponding author by request. The responsibility for scientific accuracy and content remains entirely with the authors.

**Acknowledgments:** The authors express thanks to the people who helped with this work, and acknowledge the valuable suggestions from the peer reviewers.

**Conflicts of Interest:** The authors declare that the research was conducted in the absence of any commercial or financial relationships that could be construed as potential conflicts of interest.

## References

- Zhang, Z.; Ashour, A.; Ge, W.; Ni, Z.; Jiang, H.; Li, S.; Cao, D. Experimental investigation on flexural performance of steel-UHPC composite beams with steel shear keys. *Eng. Struct.* **2024**, *313*, 118275. [\[CrossRef\]](#)
- Brozzetti, J. Design development of steel-concrete composite bridges in France. *J. Constr. Steel Res.* **2000**, *55*, 229–243. [\[CrossRef\]](#)
- Kang, C.; Schneider, S.; Wenner, M.; Marx, S. Development of design and construction of high-speed railway bridges in Germany. *Eng. Struct.* **2018**, *163*, 184–196. [\[CrossRef\]](#)
- Kumar, K.N.; Anil, K.; Yogendra, S. Assessment of Dynamic Behaviour and Performance of Existing Composite Railway Bridges Under the Impact of a High-Speed LHB Train Using a Coupled Approach. *J. Vib. Eng. Technol.* **2022**, *11*, 3465–3480.
- Mato, F.M.; Santos, J.P.; Cornejo, M.O. “Arroyo Las Piedras” Viaduct: The first Composite Steel-Concrete High Speed Railway Bridge in Spain. *Struct. Eng. Int.* **2007**, *17*, 292–297. [\[CrossRef\]](#)
- Gu, Y.W.; Nie, X.; Yan, A.G.; Zeng, J.H.; Liu, Y.F.; Jiang, Y.X. Experimental and numerical study on vibration and structure-borne noise of high-speed railway composite bridge. *Appl. Acoust.* **2022**, *192*, 108757. [\[CrossRef\]](#)
- Zhou, H.; Li, H.; Chen, X.; Chen, Z.; Naser, M. Local buckling of the bottom flange in steel-concrete composite beams with trapezoidal corrugated webs subjected to end restraint at high temperatures. *Structures* **2024**, *65*, 106718. [\[CrossRef\]](#)
- Shariati, M.; Raeispour, M.; Naghipour, M.; Kamyab, H.; Memarzadeh, A.; Nematzadeh, M.; Toghroli, A. Flexural behavior analysis of double honeycomb steel composite encased concrete beams: An integrated experimental and finite element study. *Case Stud. Constr. Mater.* **2024**, *20*, e03299. [\[CrossRef\]](#)
- Liang, J.; Zou, W.; Wang, C.; Li, W. Flexural performance of partially encased steel-concrete composite beams with web opening. *Structures* **2024**, *64*, 106666. [\[CrossRef\]](#)
- Willis, R. Preliminary essay to the appendix B: Experiments for determining the effects produced by causing weights to travel over bars with different velocities. In *Report of the Commissioners Appointed to Inquire into the Application of Iron to Railway Structures*; William Clowes and Sons: London, UK, 1849.
- Stokes, G.G. Discussion of a differential equation relating to the breaking of railway bridges. *Trans. Camb. Philos. Soc.* **1849**, *8*, 707–735.
- Krylov, A.N. Mathematical collection of papers of the Academy of Sciences. *Math. Ann.* **1905**, *61*, 211.
- Timoshenko, S. On the forced vibrations of bridges. *Philos. Mag. Ser.* **1922**, *6*, 1018–1019. [\[CrossRef\]](#)
- Timoshenko, S. Vibrations of bridges. *ASME Trans.* **1928**, *49–50*, 121009. [\[CrossRef\]](#)
- Inglis, C.E. *A Mathematical Treatise on Vibration of Railway Bridges*; Cambridge University Press: Cambridge, UK, 1934.
- Matsuura, H. Interaction between vehicles and bridge girders on high-speed railways. *Railw. Tech. Res. Rep.* **1974**, *31*, 14–17.
- Chu, K.H.; Garg, V.K.; Wiriyaichai, A. Dynamic Interaction of Railway Train and Bridges. *Veh. Syst. Dyn.* **2007**, *9*, 207–236. [\[CrossRef\]](#)
- Wiriyaichai, A.; Chu, K.H.; Garg, V.K. Bridge Impact due to Wheel and Track Irregularities. *J. Eng. Mech. Div.* **1982**, *108*, 648–666. [\[CrossRef\]](#)
- Bhatti, M.H. Vertical and Lateral Dynamic Response of Railway Bridge Due to Nonlinear Vehicle and Track Irregularities. Chicago. Ph.D. Thesis, Illinois Institute of Technology, Chicago, IL, USA, 1982.
- Wang, T.L.; Chu, K.H. Railway bridge/vehicle interaction studies with new vehicle model. *Struct. Eng.* **1991**, *117*, 2099–2116. [\[CrossRef\]](#)
- Liu, X.; Wu, H.; Zhao, S.; Yang, X. Experimental analysis of rotating bridge structural responses to existing railway train loads via time-frequency and Hilbert–Huang transform energy spectral analysis. *Sci. Rep.* **2024**, *14*, 8385. [\[CrossRef\]](#)

22. König, P.; Adam, C. A model considering the longitudinal track–bridge interaction in ballasted railway bridges subjected to high-speed trains. *Acta Mech.* **2023**, *235*, 1395–1418. [[CrossRef](#)]
23. König, P.; Salcher, P.; Adam, C.; Hirzinger, B. Dynamic analysis of railway bridges exposed to high-speed trains considering the vehicle–track–bridge–soil interaction. *Acta Mech.* **2021**, *232*, 4583–4608. [[CrossRef](#)]
24. Moritoh, Y.; Zenda, Y.; Nagakura, K. Noise control of high speed shinkansen. *J. Sound Vib.* **1996**, *193*, 319–334. [[CrossRef](#)]
25. Wang, A.; Cox, S.; Gosling, D.; Prudhoe, J. Railway bridge noise control with resilient baseplates. *J. Sound Vib.* **2000**, *231*, 907–911. [[CrossRef](#)]
26. Ngai, K.W.; Ng, C.F. Structure-borne noise and vibration of concrete box structure and rail viaduct. *J. Sound Vib.* **2001**, *255*, 281–297. [[CrossRef](#)]
27. Poisson, F.; Margiocchi, F. The use of dynamic dampers on the rail to reduce the noise of steel railway bridges. *J. Sound Vib.* **2005**, *293*, 944–952. [[CrossRef](#)]
28. Zhang, X.; Zhang, X.; Song, G.; Xu, J.; Yang, L. Key Mechanism Research of Top Plate Thickening of the Box-Girder Bridge for Noise Reduction Design in High-Speed Railway. *Appl. Sci.* **2023**, *13*, 8958. [[CrossRef](#)]
29. Zhang, X.; Zhang, X.; Yang, J.; Zhu, S.; He, Q. Mechanism of noise reduction caused by thickening top plate for high-speed railway box-girder bridge. *Structures* **2023**, *57*, 105148. [[CrossRef](#)]
30. Li, X.; Zhang, X.; Zhang, Z.; Liu, Q.; Li, Y. Experimental research on noise emanating from concrete box-girder bridges on intercity railway lines. *Proc. Inst. Mech. Eng. Part F J. Rail Rapid Transit* **2015**, *229*, 125–135. [[CrossRef](#)]
31. Zhang, X.; Li, X.; Liu, Q.; Wu, J.; Li, Y. Theoretical and experimental investigation on bridge-borne noise under moving high-speed train. *Sci. China Technol. Sci.* **2013**, *56*, 917–924. [[CrossRef](#)]
32. Li, Q.; Xu, Y.L.; Wu, D.J. Concrete bridge-borne low-frequency noise simulation based on train–track–bridge dynamic interaction. *J. Sound Vib.* **2012**, *331*, 2457–2470. [[CrossRef](#)]
33. Liu, X.; Zhang, N.; Sun, Q.; Wu, Z. Experimental and numerical study on vibration and structure-borne noise of composite box-girder railway bridges. *Int. J. Rail Transp.* **2024**, *12*, 134–152. [[CrossRef](#)]
34. Liu, Q. Prediction of Structure-Borne Noise from Railway Composite Bridge and Suppression Study of Constrained Layer Damping. Ph.D. Thesis, Southwest Jiaotong University, Chengdu, China, 2015.
35. Li, X.; Liu, Q.; Pei, S.; Song, L.; Zhang, X. Structure-borne noise of railway composite bridge: Numerical simulation and experimental validation. *J. Sound Vib.* **2015**, *353*, 378–394. [[CrossRef](#)]
36. Du, M.; Wang, K.; Ge, X.; Zhang, X. Bridge-Borne Noise Induced by High-Speed Freight Electric Multiple Units: Characteristics, Mechanisms and Control Measures. *Appl. Sci.* **2024**, *14*, 2801. [[CrossRef](#)]

**Disclaimer/Publisher’s Note:** The statements, opinions and data contained in all publications are solely those of the individual author(s) and contributor(s) and not of MDPI and/or the editor(s). MDPI and/or the editor(s) disclaim responsibility for any injury to people or property resulting from any ideas, methods, instructions or products referred to in the content.